nature portfolio

https://doi.org/10.1038/s41567-021-01229-9

Supplementary information

Competition and interplay between topology and quasi-periodic disorder in Thouless pumping of ultracold atoms

In the format provided by the authors and unedited

Supplementary Information for: Competition and interplay between topology and quasi-periodic disorder in Thouless pumping of ultracold atoms

Shuta Nakajima,[1,2] Nobuyuki Takei,[1] Keita Sakuma,[1]
Yoshihito Kuno,[1,3] Pasquale Marra,[4,5] and Yoshiro Takahashi[1]

[1]*Department of Physics, Graduate School of Science, Kyoto University, Kyoto 606-8502, Japan*

[2]*The Hakubi Center for Advanced Research, Kyoto University, Kyoto 606-8502, Japan*

[3]*Department of Physics, University of Tsukuba, Tsukuba, Ibaraki 305-8571, Japan*

[4]*Graduate School of Mathematical Sciences, The University of Tokyo, Komaba, Tokyo, 153-8914, Japan*

[5]*Department of Physics, and Research and Education Center for Natural Sciences, Keio University, Hiyoshi, Kanagawa, 223-8521, Japan*

(Dated: March 5, 2021)

S1. APPROXIMATED TIGHT-BINDING MODEL

In order to estimate the qualitative properties of our experimental system modeled by the cRM model, we consider an approximated tight-binding picture. Our experimental system is based on the following dynamical superlattice potential in a clean limit:

$$V_{\rm clean}(x,t) = -V_S \cos^2\left(\frac{2\pi x}{d}\right) - V_L \cos^2\left(\frac{\pi x}{d} - \phi(t)\right). \tag{S1}$$

Hereafter, since in our experiments only the first band is almost occupied, and the band gap between the second and third bands are fairly large, we can focus on only the first and second bands created by our experimental superlattice potential. Then, we can describe the system with an effective tight-binding model, namely, the tRM model in a clean limit, which reads

$$\hat{H}_{\rm RM} = \sum_i \Big[-(J+\delta)\hat{a}_i^\dagger \hat{b}_i - (J-\delta)\hat{a}_i^\dagger \hat{b}_{i+1} + \text{h.c.} + \Delta(\hat{a}_i^\dagger \hat{a}_i - \hat{b}_i^\dagger \hat{b}_i) \Big]. \tag{S2}$$

In the topological charge pumping (TCP), δ and Δ are adiabatic dynamical parameters, which can be approximately determined by the band structure induced by the superlattice potential $V_{\rm clean}(x,t)$. Here, we approximate these dynamical sequence for δ and Δ as a circular trajectory, $\delta = \delta_0 \sin\theta$, $\Delta(t) = \Delta_0 \cos\theta$, where $\theta = 2\phi(t)$. Although the actual dynamical sequence for δ and Δ in our experimental system is subtly different from the circular one, this approximation facilitates the ideal theoretical treatment of the TCP phenomena, especially for calculating the Chern number, and can give insight for qualitative properties of the TCP described by the cRM in our experiment. The physical values of J, δ_0 and Δ_0 can be directly determined by the band structure of the superlattice potential $V_{\rm clean}(x,t)$. The values of J and δ_0 are determined by the band width in the double-well lattice case ($\theta = \pi/2,\, 3\pi/2$), while the value of Δ_0 by the band gap in the staggered lattice case ($\theta = 0,\, \pi$) as discussed in the previous study [1]. For the band structure determined by our experimental setup, the tRM parameters are approximately determined. The tRM model is expected to capture the qualitative behavior for our experimental system since, in the clean limit, the circular parameter sequence for δ and Δ is topologically connected to our actual experimental sequence without gap closing. Regarding the basic topological aspect of the tRM model, for $\Delta = 0$ (at inversion symmetric point, $\theta = \pi/2,\, 3\pi/2$), the model reduces to the celebrated Su-Schrieffer-Heeger (SSH) model, classified in the Altland-Zirnbauer class BDI of the periodic classification of topological states[2, 3]. The SSH model

exhibits a topological phase and zero energy topological edge modes [4]. However, a finite Δ breaks the chiral symmetry without gap closing, i.e., $\hat{\sigma}_z \hat{H}_{\rm RM}(k)\hat{\sigma}_z \neq -\hat{H}_{\rm RM}(k)$ where $\hat{H}_{\rm RM}(k)$ is the bulk momentum Hamiltonian of Eq. (S2). Accordingly, the tRM model is not necessarily in the BDI class.

In our experiment, a quasi-periodic disorder lattice created by an additional laser with wavelength λ_D (= 798 nm) applied by tilting 45° for the one-dimensional superlattice axis, is given by

$$V_{\rm Dis}(x) = -V_D \cos^2\left(\frac{\pi x}{d_D} + \frac{\alpha}{2}\right), \tag{S3}$$

(see Fig. 1a of the main text). This quasi-periodic disorder potential $V_{\rm Dis}(x)$ can be effectively implemented in the tRM model as an on-site potential given by

$$\hat{V}'_{\rm Dis} = \frac{\Delta_D}{2}\sin[2\pi\beta(2i)+\alpha]\hat{a}_i^\dagger\hat{a}_i + \frac{\Delta_D}{2}\sin[2\pi\beta(2i-1)+\alpha]\hat{b}_i^\dagger\hat{b}_i, \tag{S4}$$

where $\beta = d/(2d_D)$. The potential amplitude Δ_D in $\hat{V}'_{\rm Dis}$ does not strictly correspond to the value of the continuous system potential V_D but gives a good approximation. The quasi-periodic disorder potential $\hat{V}'_{\rm Dis}$ is diagonal and breaks the chiral symmetry even for $\theta = \pi/2$ or $2\pi/3$ SSH case. In general, this type of disorder strongly affects the topological system and leads to the breakdown of the topological phase, compared to a chiral symmetric disorder employed in a recent experiment [5]. On the other hand, in this tight-binding picture we ignore modulated effects of $V_{\rm Dis}(x)$ to the tRM parameters, J, δ_0 and Δ_0. Thus, we consider $\hat{H}_{RM} + \hat{V}'_{\rm Dis}$ as an approximated tight-binding model for our experimental system.

For the sake of simplicity, we consider the effect of the quasi-periodic disorder only on the on-site potential and ignore the effects of the trapping potential. However, the resulting model is nevertheless able to capture the essence of the physical behavior of the cRM model and the experimental system. In particular, for small V_D, the tRM model reasonably approximates the cRM model. However, for large V_D, deviations between the tRM model and cRM models become noticeable. Since $\hat{V}'_{\rm Dis}$ is diagonal, the total tight-binding model has no chiral symmetry even for inversion symmetric point, therefore $\hat{V}'_{\rm Dis}$ is expected to have a strong influence to the TCP.

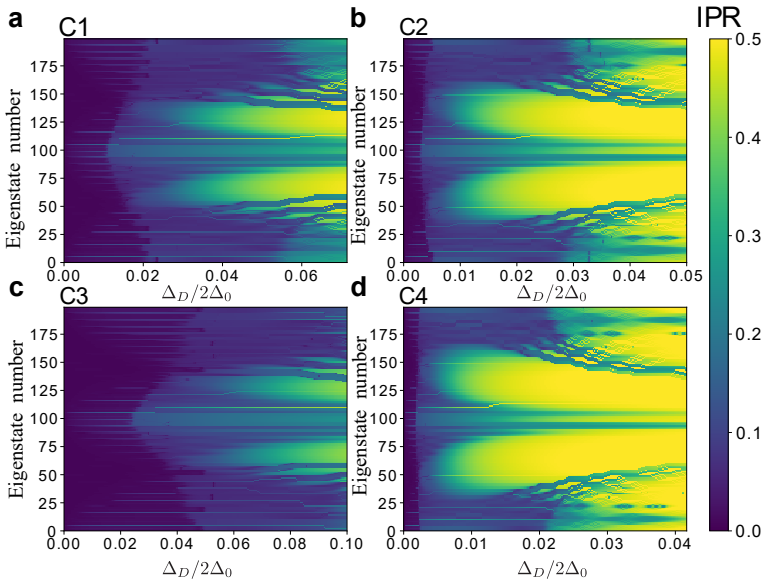

FIG. S1. **IPR calculation for a quasi-periodic disordered SSH model.** **a**, C_1: $(V_L,V_S) = (20,14)E_R$, $(J,\delta_0,\Delta_0) = (0.861,0.851,6.45)E_R$. **b**, C_2: $(V_L,V_S) = (30,20)E_R$, $(J,\delta_0,\Delta_0) = (0.860,0.857,8.54)E_R$. **c**, C_3: $(V_L,V_S) = (15,10)E_R$, $(J,\delta_0,\Delta_0) = (0.914,0.898,4.86)E_R$. **d**, C_4: $(V_L,V_S) = (36,24)E_R$, $(J,\delta_0,\Delta_0) = (0.827,0.825,9.605)E_R$.

S2. LOCALIZATION TRANSITION IN A QUASI-PERIODIC DISORDERED SSH MODEL

To estimate the Anderson localization point V_{AL} in our experimental system, we calculate effects of quasi-periodic disorder created in a disordered SSH model, corresponding to the $\Delta = 0$ case in the tRM model of Eq. (S2) including the $\hat{V}'_{\text{Dis}}$ of Eq. (S4) as an effect of the disordered lattice potential. Here, we consider a quasi-periodic disorder lattice with a wavelength of 798 nm. In general, since we consider quasi-periodic disorder, we expect an Anderson localization transition at a finite disorder strength even in the one dimensional system. In conventional Anderson localization, single atoms are localized at each single lattice site. To estimate the localization transition in our considering system, we employ the inverse participation ratio (IPR). The IPR for each eigenstate is defined as

$$(\text{IPR})_\ell = \sum_j |\langle j|\psi_\ell\rangle|^4, \tag{S5}$$

where $|j\rangle$ is a j-site localized single-particle state and $|\psi_\ell\rangle$ is ℓ-th eigenstate in the SSH model with quasi-periodic disorder potential. A large value of the IPR is a signature of

the localized tendency of the single-particle wave function. We perform the IPR calculation for four different parameter sets of (J,δ) corresponding to those in the four different pump trajectories in our experiments. The results are shown in Fig. S1, where we plot the IPR as a function of Δ_D and of the eigenstate number in $L = 200$ lattice site system with periodic boundary conditions. The sets C_1 and C_2 correspond to the parameter sets A and B in Fig. 2a in the main text, and the set C_3 and C_4 correspond to the trajectories $C_{\rm inner}$ and $C_{\rm outer}$ in Fig. 4b, respectively. The order of the eigenstate numbers corresponds to the eigenenergy in ascending order. Due to the quasi-periodic disorder, all cases in Fig. S1 exhibit mobility edges, i.e., different eigenstates localize for different disorder strengths. Here we take the condition $({\rm IPR})_\ell \gtrsim 0.1$ as a localization criterion, while the transition point is determined by the case where all eigenstates fulfill this condition. For all the cases in Fig. S1, all the eigenstates already tend to be localized for $\Delta_D/2\Delta_0 < 0.04$. We define the Anderson localization transition point V_{AL} in the main text, using eigenstates with lower eigenenergies. These states are localized at $\Delta_D/2\Delta_0 \sim 0.02$ and $\Delta_D/2\Delta_0 \sim 0.004$ for the pump trajectories C_1 and C_2 (or the set A and B in the main text), respectively. These values correspond to $V_{AL}^A \sim 0.3E_R$ and $V_{AL}^B \sim 0.07E_R$. Even though from the numerical calculation our experimental system (cRM model) is also expected to be localized around the SSH parameters points, this fact does not mean gap closing directly. Even when the system exhibits localization and fulfills our criteria, the pumping does not necessarily break down, as shown numerically in Ref. [6].

S3. CHERN NUMBER CALCULATION FROM A DIMENSIONAL EXTENDED TIGHT-BINDING MODEL

The tRM model can be mapped into the Harper–Hofstadter–Hatsugai (HHH) model [7] through a dimensional extension [8, 9]. By regarding the pumping parameter θ in $\hat{H}_{\rm RM}$ of Eq. (S2) as y-direction momentum k_y and applying the Fourier transformation for k_y, we can obtain the HHH model from the tRM model:

$$\begin{aligned}\hat{H}_{2D} = \sum_{m,n}\Big[&-J\hat{c}^\dagger_{m+1,n}\hat{c}_{m,n} - \frac{\Delta_0}{2}e^{-i\pi(m-1/2)}\hat{c}^\dagger_{m,n+1}\hat{c}_{m,n} \\ &-\frac{\delta_0}{2}e^{i\pi m}\hat{c}^\dagger_{m+1,n+1}\hat{c}_{m,n} - \frac{\delta_0}{2}e^{-i\pi m}\hat{c}^\dagger_{m+1,n}\hat{c}_{m,n+1} + {\rm h.c.}\Big]. \end{aligned} \tag{S6}$$

Here $\hat{c}^{(\dagger)}_{m,n}$ is the annihilation (creation) operator at a two dimensional lattice site (m, n), where $m = 1, 2, \cdots, L_x$ and $n = 1, 2, \cdots, L_y$, i.e., $L_x \times L_y$ lattice system. The HHH model is known to have two topological bands with a non-zero Chern number [7, 8]. This is a peculiar property compared to a conventional quantum Hall system on lattice described by the Hofstadter model [10], since the Hofstadter model does not exhibit two separated bands with non-trivial topology. The two topological bands with a non-zero Chern number in the HHH model are the origin of the TCP in the tRM model. The value of the Chern number corresponds to the total pumped current per one pumping cycle in the tRM model [4]. For the HHH model, we can further implement the effect of the quasi-periodic disorder $\hat{V}'_{dis}$ of the tRM model as $\hat{V}''_{\rm Dis} = \frac{\Delta_D}{2}\sin(2\pi\beta m + \alpha)\hat{c}^\dagger_{n,m}\hat{c}_{n,m}$. Here, it should be noted that $\hat{V}''_{\rm Dis}$ depends only on the x-component site m and is uniform along y-direction.

In our experimental system, atoms almost occupy the lowest band and the occupation of atoms in higher bands is fairly suppressed. We assume that the lower band of the tRM model is fully-occupied approximately. Accordingly, in the numerical calculation of the HHH model, the half-filling case is considered. Then, to make a comparison with the experimental results shown in the main text, we set the HHH model parameters (J, δ_0, Δ_0) to four experimental parameter sets: (I) $(V_L,V_S) = (20, 14)E_R$, $(J,\delta_0,\Delta_0) = (0.861, 0.851, 6.45)E_R$, (II) $(V_L,V_S) = (30, 20)E_R$, $(J,\delta_0,\Delta_0) = (0.860, 0.857, 8.54)E_R$, (III) $(V_L,V_S) = (15, 10)E_R$, $(J,\delta_0,\Delta_0) = (0.914, 0.898, 4.86)E_R$, and (IV) $(V_L,V_S) = (36, 24)E_R$, $(J,\delta_0,\Delta_0) = (0.827, 0.825, 9.605)E_R$. These approximated circular pumping trajectories determined by the above four parameter sets are denoted by C_1, C_2, C_3 and C_4. These parameter sets (J, δ_0, Δ_0) are determined by comparing to the energy spectra of the cRM model as in the previous paper [1]. The C_1 and C_2 trajectories are the approximated version of the set A and B in the experimental pumping sequences in Fig. 2a in the main text, respectively. The C_3 and C_4 trajectories correspond to the experimental pumping sequences $C_{\rm inner}$ and $C_{\rm outer}$ in Fig. 4b, respectively. In what follows, We numerically calculated the Chern number for C_1, C_3 and C_4 trajectories and use $L_x = 40$ (20 unit cells). This x-direction system size is close to our experimental system.

We calculate the Chern number for the model of $\hat{H}_{2D} + \hat{V}''_{\rm Dis}$ in the following manner. Since discrete translational invariance is broken due to the term $\hat{V}''_{\rm Dis}$, we employ a calculation method to obtain the Chern number from the real space Hamiltonian, namely, the so-called coupling matrix method [11–14]. In this method, we impose twisted periodic boundary

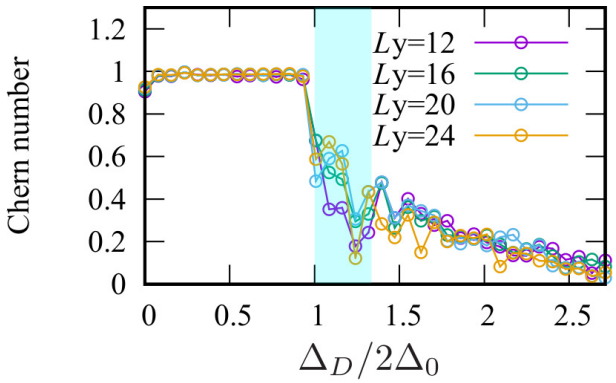

FIG. S2. **Numerical calculation of Chern number in the presence of quasi-periodic disorder and its dependence on L_y.** L_x is fixed to 40. We average over 20 different values of α, the tRM parameters are set to the C_1 case. The blue shaded regime represents a theoretically expected phase transition regime, where the TCP is suddenly suppressed.

conditions with two twisted phases θ_x and θ_y for each spatial direction. Their twisted phases play a role of the momentum k_x and k_y (corresponding to θ) in the TKNN formula [15]. Since these twisted phase boundary conditions can be employed even for a system without translational invariant such as a disordered system, we can calculate the Chern number for the model of $\hat{H}_{2D} + \hat{V}''_{\mathrm{Dis}}$.

Figure S2 displays the calculated Chern number in the presence of quasi-periodic disorder and its dependence of the artificial y-spatial system size L_y with fixed $L_x = 40$ (20 unit cells system from the viewpoint of the tRM model). The result indicates that the system-size dependence is fairly small, and the topological phase transition point does not depend much on the value of L_y. Therefore, the system size used in the numerical calculation is large enough to capture the behavior of our experimental system. $L_y = 24$ data in Fig. S2 is displayed in Fig. 2b in the main text.

Next, we employ this numerical method to study the disorder-induced charge pump (DICP). The schematic pumping trajectory plotted in the $\delta - \Delta$ plane is shown in Fig. S3a. This trajectory is a combination of circular C_3 and C_4 trajectories. Our experiment is conducted with a trajectory similar to this schematic trajectory. In particular, the experimental trajectory can be connected by continuous deformation, and it is therefore topologically equivalent, to the trajectory shown in Fig. S3a. The DICP trajectory does not wrap the origin $(\Delta_0, \delta_0) = (0, 0)$ corresponding to the gap closing point in the tRM model in the clean

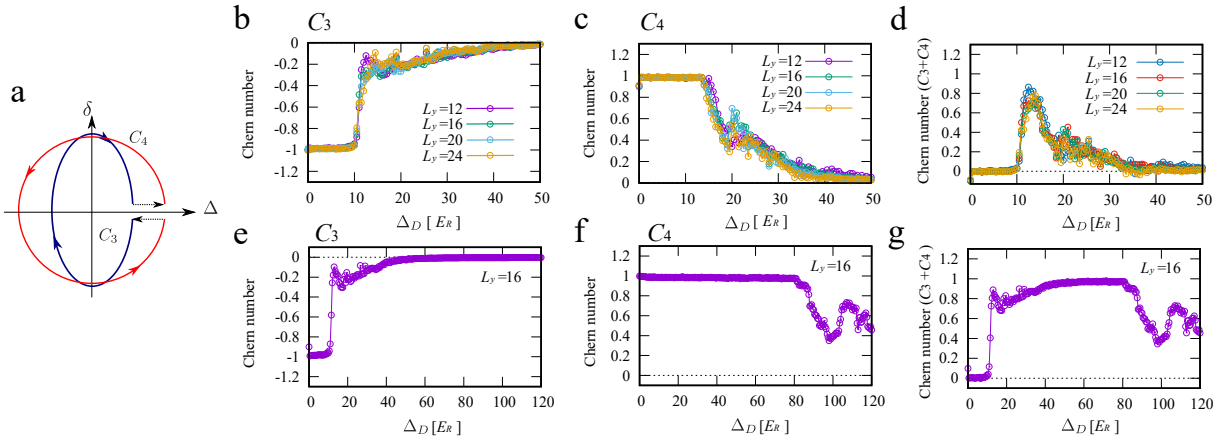

FIG. S3. **Numerical calculation of Chern number in the disorder-induced charge pumping (DICP). a**, Pumping trajectory. This is created by combining the two circular trajectories C_3 and C_4 with different circular direction. The two trajectories are connected by changing the staggered potential Δ_0 with fixed $\delta = 0$. The total pumping trajectory does not wrap the origin corresponding to the gap closing point of the clean RM model. Without the quasi-periodic disorder lattice, the total charge pumping along this trajectory is zero. **b**, Chern number behavior for C_3 trajectory and **c**, for C_4 trajectory as a function of Δ_D. The TCP in C_4 case is more robust than in C_3 trajectory. **d**, The difference of the Chern number between C_3 and C_4 trajectories as a function of Δ_D. The numerical result indicates a possibility to exhibit a disorder-induced pumping for $10E_R \lesssim \Delta_D \lesssim 30E_R$. L_y-system size dependence is fairly small. For the case that the inner (C_3) and outer (C_4) trajectories are farther apart: **e**, Chern number behavior for C_3 trajectory and **f**, for C_4 trajectory as a function of Δ_D. The TCP in C_4 case is much more robust than in C_3 trajectory. **g**, the difference of the Chern number between C_3 and C_4 trajectories as a function of Δ_D. The numerical result indicates the possibility to realize a topological DICP for $40E_R \lesssim \Delta_D \lesssim 80E_R$, where a clear quantized plateau appears.

limit. In this sense, in the clean limit, the tight-binding RM model of Eq. (S2) exhibits no TCP, i.e., the total pumped current is zero. However, once the quasi-periodic disorder $\hat{V}'_{\rm Dis}$ is switched on, the disordered model has a possibility to exhibit a non-trivial pumped current that could not occur at the clean limit. This corresponds to the fact that the disordered HHH model also has a possibility to exhibit a topological non-trivial phase with a non-vanishing Chern number, $C_N \neq 0$.

To study the DICP, we split the DICP trajectory into two circles, C_3 and C_4. For each

circular trajectory, we calculate the Chern number by using the disordered HHH model. Here, various system sizes for L_y are calculated to check the finite-size effects. Moreover, for all data, we average over different samples corresponding to different values of α (60 samples). The numerical results for each trajectory are shown in Fig. S3b and c. The data display Δ_D-dependence (not $2\Delta_0$ scale) of the Chern number. Furthermore, Fig. S3d shows the sum of the Chern number between C_3 and C_4 trajectories. The result clearly captures the presence of a non-trivial pump between $10E_{\rm R} \lesssim \Delta_D \lesssim 30E_{\rm R}$, quantified by the imperfect cancellation between the Chern numbers for C_3 and C_4 trajectories. All results in Fig. S3b-d indicate that the finite system size (L_y) dependence is fairly small. $L_y = 24$ data in Fig. S3 are used in Fig. 4b and c in the main text.

In addition, we show that this type of pump protocol in Fig. S3a theoretically exhibits a topological DICP. Here, we consider that the inner and outer trajectories are farther apart compared with the experimental ones, i.e., we set the inner circle (C3) with $(J, \delta_0, \Delta_0) = (1, 0.9, 5)E_R$ and the outer circle (C4) with $(J, \delta_0, \Delta_0) = (6, 5, 45)E_R$. The numerical results are shown in Fig. S3e-g. As seen in Fig.S3g, there exists a quantized plateau within the errors or fluctuations due to numerical instability inevitable for disordered systems for moderate disorder strength.

S4. CONTINUOUS MODEL

To obtain the band structure in the continuous system, we use a continuous model with a lattice potential given by

$$V(x,t) = -V_{\rm S}\cos^2\left(\frac{2\pi x}{d}\right) - V_{\rm L}\cos^2\left(\frac{\pi x}{d} - \phi(t)\right) - V_{\rm D}\cos^2\left(\frac{\pi x}{d_{\rm D}} + \frac{\alpha}{2}\right), \tag{S7}$$

and we solve the time-independent Schrödinger equation

$$\left[-\frac{\hbar^2\partial_x^2}{2m} + V(x,\phi)\right]\Psi(x,t) = E\Psi(x,t), \tag{S8}$$

using space discretization. Using the recoil energy as the energy unit and the lattice constant of the long lattice as the length unit one has $E_R = h^2/(8m)^2 = 1$.

Since $d_{\rm D}/d$ is an irrational number, the quasi-periodic disorder lattice is incommensurate with respect to the short and the long lattice. As a consequence, the translational symmetry of the lattice is broken, and thus the unit cell of the superlattice is not well-defined.

Hence, one cannot meaningfully define the periodic boundary conditions for the system. Therefore, we will approach the irrational value $d_{\rm D}/d = 3/2\sqrt{2}$ by taking a succession of rational approximations of the irrational number, obtained in terms of continued fraction representation [16]. Every irrational number $R \in \mathbb{R} - \mathbb{Q}$ can be written uniquely as an infinite continued fraction as

$$R = [N_0; N_1, N_2, \ldots] = N_0 + \cfrac{1}{N_1 + \cfrac{1}{N_2 + \ldots}} \tag{S9}$$

with $N_i \in \mathbb{Z}$ integers. The successive approximations R_n are obtained by truncating the continued fraction representation $[N_0; N_1, N_2, \ldots, N_n]$. Since R_n are rational numbers one can write as

$$R_n = [N_0; N_1, N_2, \ldots N_n] = \frac{P_n}{Q_n} \approx R, \tag{S10}$$

where P_n, Q_n are coprimes. These represent successive rational approximations of the irrational number R.

In our specific case one has

$$\frac{d_{\rm D}}{d} = \frac{3}{2\sqrt{2}} \approx \frac{17}{16}, \frac{35}{33}, \frac{577}{544}, \ldots = 1.0625, 1.060606060\ldots, 1.060661764\ldots, \ldots \tag{S11}$$

For $V_{\rm D} = 0$ the unit cell of the superlattice has length d. For $V_{\rm D} > 0$ and $R = d/d_{\rm D}$ being a rational number $R = P/Q$ with P, Q coprimes, the total unit cell of the superlattice has length Qd as one can see by direct substituting $x \to x + Q$ into Eq. (S7). The energy levels are then obtained by solving the Schrödinger equation with periodic boundary conditions over a system of length $L = N_{\rm c} Q d$ where $N_{\rm c}$ is the total number of unit cells. We take $P/Q = 35/33$ and a total length of $198d$.

Figure S4 shows the bulk density of states (DoS) as a function of $V_{\rm D}$ and the band structure in the clean and in the strong disorder regimes, for different values of the lattice depths $V_{\rm L}$ and $V_{\rm S}$. The DoS and the band structure are calculated using closed (periodic) boundary conditions. In the shallower lattice cases (a and b) we can clearly see from the DoS that the global gap closes and reopens at $V_{\rm D} \approx 5$. For the case (c), a very small gap closes and reopens at $V_{\rm D} \approx 7$. In the case (d), which is the same as Fig. 3d of the main text, the numerical calculations show the gap closing at $V_{\rm D} \approx 5$ but do not show such re-opening of the gap.

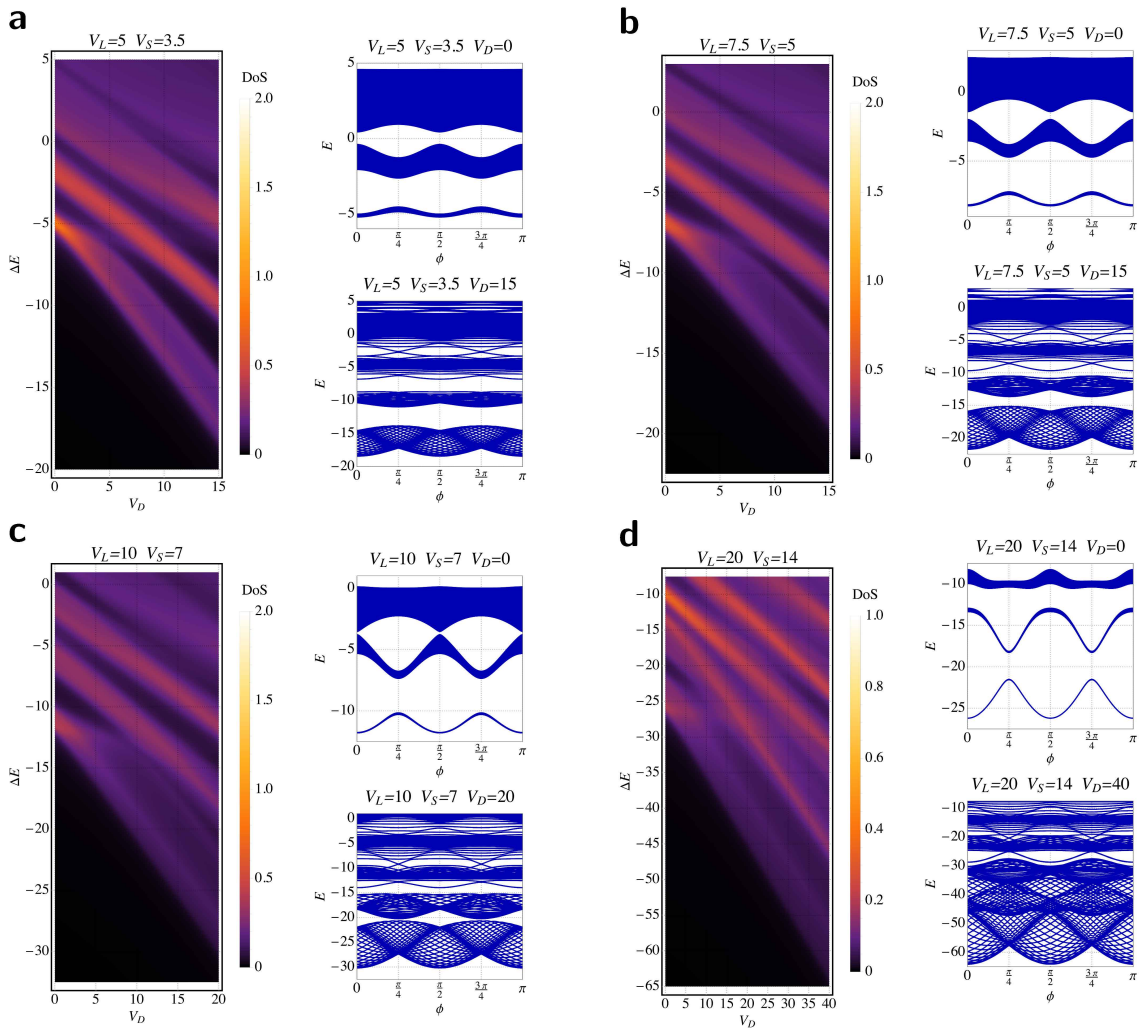

FIG. S4. **Bulk density of states (DoS) as a function of $V_{\rm D}$ and band structure in the clean and in the strong disorder regimes, for different values of the lattice depths $V_{\rm L}$ and $V_{\rm S}$.** **a**, For $V_{\rm L}, V_{\rm S} = 5, 3.5$ we can clearly see from the DoS that the global gap closes and reopens at $V_{\rm D} \approx 5$. **b**, Also for $V_{\rm L}, V_{\rm S} = 7.5, 5$ we can clearly see that the global gap closes and reopens at $V_{\rm D} \approx 5$. **c**, For $V_{\rm L}, V_{\rm S} = 10, 7$ the gap closes and a very small gap reopens at $V_{\rm D} \approx 7$. **d**, For $V_{\rm L}, V_{\rm S} = 20, 14$ which is the same as Fig. 3d of the main text, the gap closes at $V_{\rm D} \approx 5$ but does not reopen. We consider a system with total length equal to $198d$ and with $\alpha = 0$. The DoS is averaged over the phase ϕ.

Figure S5 shows the band structure calculated in the case of open boundary conditions in the clean $V_{\rm D} = 0$ and strong $V_{\rm D} = 15$ disorder regimes, for the parameter set $V_{\rm L}, V_{\rm S} = 5, 3.5$ (as in Fig. S4a). In the clean limit, one can clearly see an edge state which connects the lowest

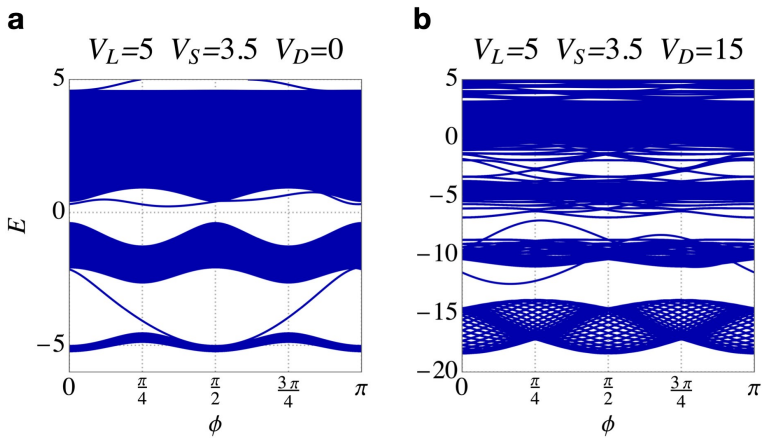

FIG. S5. **Band structure for a system with open boundary conditions with** $V_{\mathrm{L}}, V_{\mathrm{S}} = 5, 3.5$**.** **a**, In the clean limit $V_{\mathrm{D}} = 0$ there is a non-trivial edge state connecting the lowest energy band (at filling $j = 1$) with the first excited band. **b**, In the strong disorder regime $V_{\mathrm{D}} = 15$ there are no edge states connecting the lowest energy band with the first excited band.

energy band with the first excited band. Therefore the lowest energy gap is topologically non-trivial. In the strong disorder case, there is an intraband state in the lowest energy gap. This intraband state does not connect the two bands and it is therefore topologically trivial. Non-trivial edge states are also present in the lowest energy gap in the clean limit $V_{\mathrm{D}} = 0$ for $V_{\mathrm{L}}, V_{\mathrm{S}} = 7.5, 5$, $V_{\mathrm{L}}, V_{\mathrm{S}} = 10, 7$, and $V_{\mathrm{L}}, V_{\mathrm{S}} = 20, 14$. However, for these choices of the lattice depths, the energy band dispersion becomes so broad that the lowest energy gaps become very narrow, and the presence and identification of intraband edge states cannot be resolved unambiguously.

S5. EVALUATION OF EXCITATION FRACTION

In Fig. 3a of the main text, we investigate the gap closing between the first and second bands by measuring the fraction of atoms excited to the second band after three cycles of cRM pumping under quasi-periodic disorder with the lattice parameter $(V_L, V_S) = (20, 14)E_R$. The band structure is defined for the long lattice, spanned by the quasi-momentum q, since we adiabatically turn off the quasi-periodic disorder lattice from the whole lattice setup in 130 ms. We then utilize a band-mapping technique, where an adiabatic turn-off of the remaining optical lattices maps quasi-momentum q of n-th band to

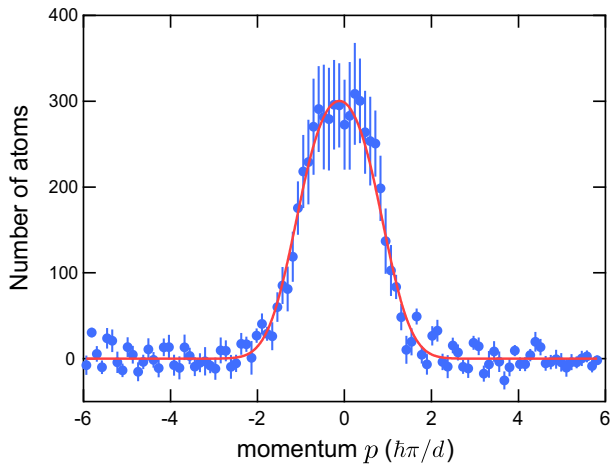

FIG. S6. **Measured momentum distribution of atoms in the case of a clean limit with ϕ fixed at 0.** It is fitted with the function $f_1(p)$ defined in Eq. (S12). Error bars denote the standard deviation of ten independent measurements.

free-particle momentum p of n-th Brillouin zone [17, 18]. By taking absorption images after time-of-flight of 10 ms, we evaluate atom fractions in the first and second bands from the momentum distribution.

In the case of a clean limit with ϕ fixed at 0, it is expected that only the first band is occupied. Figure S6 shows the measured momentum distribution corresponding to this case. An almost homogeneous distribution is obtained within the first Brillouin zone. However, the homogenous distribution was smoothed around $p = \pm\hbar\pi/d$ owing to experimental imperfection such as non-adiabaticity in the band mapping. We approximate this smoothing by the following function $f_1(p)$:

$$f_1(p) = \frac{a}{2}\left[\mathrm{erf}\left(\frac{p+\pi/d}{s}\right) + \mathrm{erf}\left(-\frac{p-\pi/d}{s}\right)\right], \tag{S12}$$

here a and s are fitting parameters and the fitted s value s_{fit} denotes the smoothness. We assume that this fitted function represents the momentum distribution when the first band is homogeneously occupied.

During the pumping under the quasi-periodic disorder, atoms can be excited to the second band. Suppose that the atom distribution in the second band is also homogeneous, and the smoothness of the value s_{fit} obtained above is common for both the first and second bands. Then we fit the measured data for the pumping under the quasi-periodic disorder using the

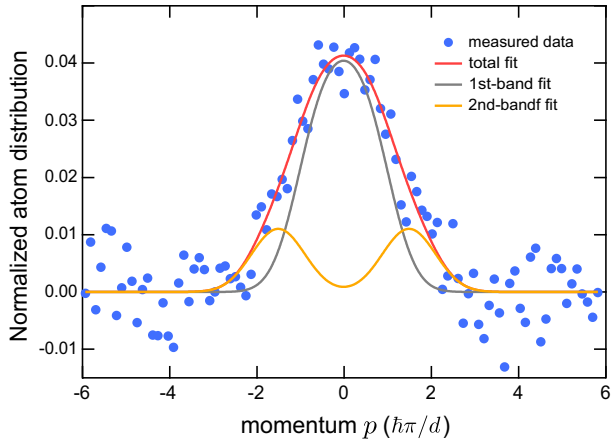

FIG. S7. **Measured momentum distribution of atoms after the Thouless pumping under the quasi-periodic disorder.** This is one typical example of ten independent measurements obtained at the disorder $V_D = 20E_R$. It is fitted with the functions $f_t(p)$, defined in Eq. (S13), for the whole band (red), $f_1(p)$ for the first band (grey), and $f_2(p)$ for the second band (orange). The vertical axis is normalized such that the integral of the fitted $f_t(p)$ is unity. The whole shift in the horizontal axis is corrected such that the functions are symmetric with respect to $p = 0$.

following function $f_t(p)$:

$$f_t(p) = f_1(p) + f_2(p), \tag{S13}$$

here

$$f_2(p) = \frac{b}{2}\left[\mathrm{erf}\left(\frac{p+2\pi/d}{s_{\mathrm{fit}}}\right) + \mathrm{erf}\left(-\frac{p+\pi/d}{s_{\mathrm{fit}}}\right)\right] + \frac{b}{2}\left[\mathrm{erf}\left(\frac{p-\pi/d}{s_{\mathrm{fit}}}\right) + \mathrm{erf}\left(-\frac{p-2\pi/d}{s_{\mathrm{fit}}}\right)\right], \tag{S14}$$

and b is a fitting parameter. The fitted functions $f_1(p)$ and $f_2(p)$ show the momentum distributions in the first and second bands, respectively. Figure S7 shows one of the fitted results at the disorder $V_D = 20E_R$ in Fig. 3a in the main text. After normalizing the integral of the fitted $f_t(p)$, we evaluated the second-band fraction by calculating $\int dp f_2(p)$. The mean and error bar representing the standard deviation in Fig. 3a of the main text are obtained for ten independent measurements at each disorder strength.

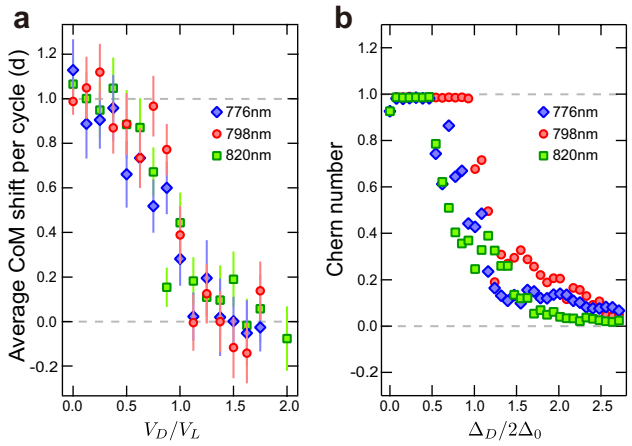

FIG. S8. **Dependence of pumping suppression on the wavelength of the quasi-periodic disorder lattice.** **a**, The CoM shift per cycle averaged after three cycles plotted as a function of the normalized depth of the disorder lattice with wavelength of $\lambda_D = 776$ nm (blue diamond), 798 nm (red circle), and 820 nm (green square) for cRM lattice with $(V_L, V_S) = (20, 14)E_R$. The error bars denote the 1σ confidence bound derived from more than forty CoM measurements. **b**, Numerical calculation of the wavelength dependence of the Chern number, plotted as a function of the normalized disorder strength in the tight-binding model. The symbols are the same as those in **a**.

S6. DEPENDENCE OF PUMPING SUPPRESSION ON DISORDER-LATTICE WAVELENGTH

We examine the dependence of the pumping suppression on the wavelength of the disorder lattice λ_D. Figure S8a shows the pumping amounts measured at quasi-periodic disorder wavelengths $\lambda_D = 776$ nm (red diamond), 798 nm (blue circle), and 820 nm (green square). The data at 798 nm are the same as those with the set A in Fig. 2 in the main text. There is no clear difference among the results for those different wavelengths. Our numerical calculation with a tRM model supports the tendency of the measured results (see Fig. S8b). As one can see, the charge pumping starts to decrease from one at a certain critical disorder strength, which depends on the wavelength. However, the pumping is largely suppressed at almost the same value $V_D \gtrsim 20E_R$ for all three wavelengths.

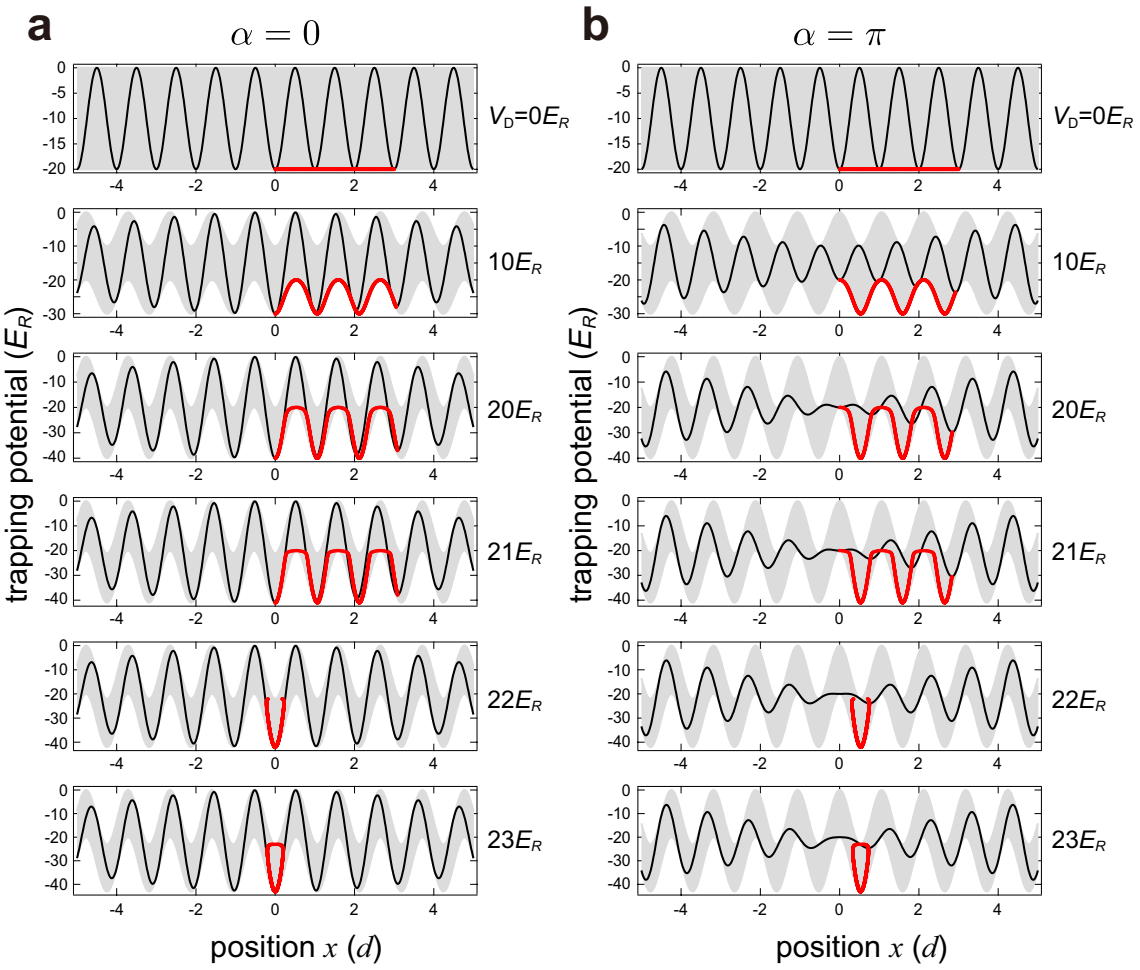

FIG. S9. **Position change of the local minimum point in the trapping potential with long and quasi-periodic disorder lattices.** The long-lattice depth is fixed to $V_L = 20E_R$, whereas the disorder strength V_D is changed as described on the right side. The quasi-periodic disorder phase α is set to 0 (**a**) or π (**b**). The phase $\phi(t)$ is swept from 0 to 3π, corresponding to three pump cycles. The black line shows the initial potential at $\phi(0) = 0$, and the gray shaded area represents the region in which the trapping potential moves during the three cycles. The position change of the local minimum point of the trap, initially located at $x \approx 0$, is depicted as the red line.

S7. INTUITIVE UNDERSTANDING OF PUMP SUPPRESSION

We can understand intuitively why the pump is suppressed at $V_D \sim V_L$ in the following way. As long as the lowest band is occupied, Thouless pumping with a cRM lattice is topologically equivalent to that only with a sliding long lattice [1]. Therefore we can capture the

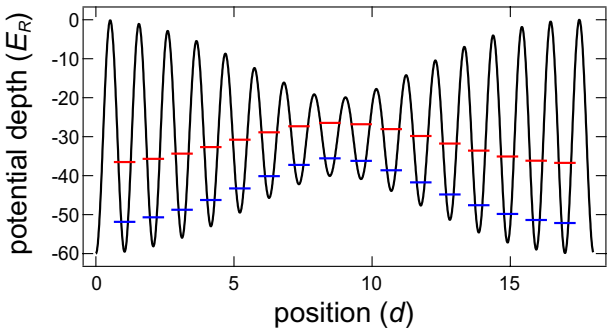

FIG. S10. **Trapping potential created by the long and quasi-periodic disorder lattices.** Their trap depths are set to $V_L = 20E_R$ and $V_D = 40E_R$, respectively, and the relative phase is zero at the origin. The ground and first-excited vibrational levels are schematically indicated by blue and red bars, respectively.

essence of the results of the pump suppression by considering a sliding lattice superimposed with a quasi-periodic disorder lattice, namely the second and third terms of Eq (1) in the main text.

Figure S9 shows the trapping potential produced by these two lattices as a function of position x. In addition, the position change of the local minimum point of the trap during three pump cycles is depicted by the red line. The trap depth of the long lattice is fixed to $V_L = 20E_R$, whereas the disorder strength V_D is varied from $0E_R$ to $23E_R$ (from top to bottom). When $V_D \leq 21E_R$, the local minimum point moves across several lattice sites during the pump cycle in accordance with the sliding lattice. This means that the whole lattice is sliding with the phase ϕ swept. For $V_D \geq 22E_R$, however, the minimum point stops moving and wanders around the particular trap minimum. Accordingly, the whole lattice does not slide. This transition happens around $V_D \sim V_L$. Therefore it is expected that the pump is suppressed at $V_D \sim V_L$. Because this discussion does not depend largely on the wavelength of the quasi-periodic disorder lattices, it is reasonable that we observe no clear difference among the three measurements in Fig. S8.

Since the dominant lattice is that of the static quasi-periodic disorder lattice in the case of $V_D > V_L$, the above-mentioned situation also indicates that the trivial band gap should be open. Although the re-opening of the gap is not clearly visible in the numerical calculations in Fig. 3 in the main text, this does not necessarily mean that the state is metallic. In fact, the energy difference between the ground and first-excited vibrational levels within

individual lattice sites becomes large in the strong disorder as shown in Fig. S10. This large local energy gap should suppress the excitations to higher levels as observed in Fig. 3a in the main text.

---

[1] Nakajima, S. *et al.* Topological thouless pumping of ultracold fermions. *Nature Physics* **12**, 296 (2016).

[2] Schnyder, A. P., Ryu, S., Furusaki, A. & Ludwig, A. W. W. Classification of topological insulators and superconductors in three spatial dimensions. *Phys. Rev. B* **78**, 195125 (2008).

[3] Kitaev, A. Periodic table for topological insulators and superconductors. *AIP Conference Proceedings* **1134**, 22–30 (2009).

[4] Asbóth, J. K., Oroszlány, L. & Pályi, A. A short course on topological insulators. *Lecture notes in physics* **919** (2016).

[5] Meier, E. J. *et al.* Observation of the topological anderson insulator in disordered atomic wires. *Science* **362**, 929–933 (2018).

[6] Wauters, M. M., Russomanno, A., Citro, R., Santoro, G. E. & Privitera, L. Localization, topology, and quantized transport in disordered Floquet systems. *Phys. Rev. Lett.* **123**, 266601 (2019).

[7] Hatsugai, Y. & Kohmoto, M. Energy spectrum and the quantum hall effect on the square lattice with next-nearest-neighbor hopping. *Phys. Rev. B* **42**, 8282–8294 (1990).

[8] Kraus, Y. E., Lahini, Y., Ringel, Z., Verbin, M. & Zilberberg, O. Topological states and adiabatic pumping in quasicrystals. *Phys. Rev. Lett.* **109**, 106402 (2012).

[9] Lohse, M., Schweizer, C., Zilberberg, O., Aidelsburger, M. & Bloch, I. A thouless quantum pump with ultracold bosonic atoms in an optical superlattice. *Nature Physics* **12**, 350 (2016).

[10] Hofstadter, D. R. Energy levels and wave functions of bloch electrons in rational and irrational magnetic fields. *Phys. Rev. B* **14**, 2239–2249 (1976).

[11] Zhang, Y.-F. *et al.* Coupling-matrix approach to the chern number calculation in disordered systems. *Chinese Physics B* **22**, 117312 (2013).

[12] Castro, E. V., López-Sancho, M. P. & Vozmediano, M. A. H. Anderson localization and topological transition in chern insulators. *Phys. Rev. B* **92**, 085410 (2015).

[13] Sriluckshmy, P. V., Saha, K. & Moessner, R. Interplay between topology and disorder in a

two-dimensional semi-dirac material. *Phys. Rev. B* **97**, 024204 (2018).

[14] Kuno, Y. Disorder-induced chern insulator in the harper-hofstadter-hatsugai model. *Phys. Rev. B* **100**, 054108 (2019).

[15] Niu, Q., Thouless, D. J. & Wu, Y.-S. Quantized hall conductance as a topological invariant. *Phys. Rev. B* **31**, 3372–3377 (1985).

[16] Hardy, G. H. & Wright, E. M. *An Introduction to the Theory of Numbers* (Oxford University Press, Oxford, 2008), 6 edn. See chapters 10 and 11.

[17] Greiner, M., Bloch, I., Mandel, O., Hänsch, T. W. & Esslinger, T. Exploring phase coherence in a 2d lattice of bose-einstein condensates. *Phys. Rev. Lett.* **87**, 160405 (2001).

[18] Köhl, M., Moritz, H., Stöferle, T., Günter, K. & Esslinger, T. Fermionic atoms in a three dimensional optical lattice: Observing fermi surfaces, dynamics, and interactions. *Phys. Rev. Lett.* **94**, 080403 (2005).